

# Growth and decay of runaway electrons above the critical electric field under quiescent conditions

Cite as: Phys. Plasmas **21**, 022514 (2014); <https://doi.org/10.1063/1.4866912>

Submitted: 10 December 2013 . Accepted: 14 February 2014 . Published Online: 27 February 2014

C. Paz-Soldan, N. W. Eidietis, R. Granetz, E. M. Hollmann, R. A. Moyer, J. C. Wesley, J. Zhang, M. E. Austin, N. A. Crocker, A. Wingen, and Y. Zhu



[View Online](#)



[Export Citation](#)



[CrossMark](#)

## ARTICLES YOU MAY BE INTERESTED IN

[An ITPA joint experiment to study runaway electron generation and suppression](#)

Physics of Plasmas **21**, 072506 (2014); <https://doi.org/10.1063/1.4886802>

[Theory of runaway electrons in ITER: Equations, important parameters, and implications for mitigation](#)

Physics of Plasmas **22**, 032504 (2015); <https://doi.org/10.1063/1.4913582>

[Space dependent, full orbit effects on runaway electron dynamics in tokamak plasmas](#)

Physics of Plasmas **24**, 042512 (2017); <https://doi.org/10.1063/1.4981209>



**ULVAC**

**Leading the World with Vacuum Technology**

- Vacuum Pumps
- Arc Plasma Deposition
- RGAs
- Leak Detectors
- Thermal Analysis
- Ellipsometers

# Growth and decay of runaway electrons above the critical electric field under quiescent conditions

C. Paz-Soldan,<sup>1,a)</sup> N. W. Eidietis,<sup>2</sup> R. Granetz,<sup>3</sup> E. M. Hollmann,<sup>4</sup> R. A. Moyer,<sup>4</sup> J. C. Wesley,<sup>2</sup> J. Zhang,<sup>5</sup> M. E. Austin,<sup>6</sup> N. A. Crocker,<sup>5</sup> A. Wingen,<sup>7</sup> and Y. Zhu<sup>8</sup>

<sup>1</sup>Oak Ridge Institute for Science and Education, Oak Ridge, Tennessee 37830-8050, USA

<sup>2</sup>General Atomics, P.O. Box 85608, San Diego, California 92186-5608, USA

<sup>3</sup>Massachusetts Institute of Technology, 77 Massachusetts Ave., Cambridge, Massachusetts 02139, USA

<sup>4</sup>University of California San Diego, 9500 Gilman Dr., La Jolla, California 92093-0417, USA

<sup>5</sup>University of California Los Angeles, P.O. Box 957099, Los Angeles, California 90095-7099, USA

<sup>6</sup>University of Texas at Austin, 2100 San Jacinto Blvd, Austin, Texas 78712-1047, USA

<sup>7</sup>Oak Ridge National Laboratory, P.O. Box 2008, Oak Ridge, Tennessee 37831, USA

<sup>8</sup>University of California Irvine, University Dr., Irvine, California 92697, USA

(Received 10 December 2013; accepted 14 February 2014; published online 27 February 2014)

Extremely low density operation free of error field penetration supports the excitation of trace-level quiescent runaway electron (RE) populations during the flat-top of DIII-D Ohmic discharges. Operation in the quiescent regime allows accurate measurement of all key parameters important to RE excitation, including the internal broadband magnetic fluctuation level. RE onset is characterized and found to be consistent with primary (Dreicer) generation rates. Impurity-free collisional suppression of the RE population is investigated by stepping the late-time main-ion density, until RE decay is observed. The transition from growth to decay is found to occur 3–5 times above the theoretical critical electric field for avalanche growth and is thus indicative of anomalous RE loss. This suggests that suppression of tokamak RE avalanches can be achieved at lower density than previously expected, though extrapolation requires predictive understanding of the RE loss mechanism and magnitude. © 2014 AIP Publishing LLC.

[<http://dx.doi.org/10.1063/1.4866912>]

## I. INTRODUCTION

When the collisional drag on an electron in a torus is exceeded by the acceleration from the toroidal electric field ( $E_\phi$ ), the phenomenon of electron runaway occurs.<sup>1,2</sup> The runaway electron (RE) continually transits toroidally, gaining energy at a rate of  $\approx E_\phi c$  (where  $c$  is the speed of light), until radiative losses balance the energy gain from  $E_\phi$ . In magnetic confinement devices, this occurs at  $\mathcal{O}(10^{-2})$  MeV levels and a RE population at this energy can cause significant damage should it impact the device wall. The potential damage caused by REs is proportional to both their energy and number, both of which scale unfavorably with the parameters associated with next generation devices such as ITER.<sup>3</sup>

RE production can arise from one of two broad mechanisms.<sup>2</sup> Primary (also called conventional) generation occurs when the collisional drag on an electron is exceeded by the electric field acceleration. The thermal electron-electron collisional frequency is given by  $\hat{\nu}_{ee} = n_e e^4 \ln \Lambda / (4\pi \epsilon_0^2 m_e^2 v_{T_e}^3)$ , where  $n_e$  is the electron density,  $v_{T_e} = \sqrt{2T_e/m_e}$  is the electron thermal speed,  $T_e$  is the electron temperature, and  $\ln \Lambda$  is the Coulomb logarithm. The  $E_\phi$  at which an electron traveling at  $v_{T_e}$  will runaway is given by the Dreicer field

$$E_D = \frac{n_e e^3 \ln \Lambda}{4\pi \epsilon_0^2 T_e}. \quad (1)$$

<sup>a)</sup>Electronic mail: paz-soldan@fusion.gat.com

Steady-state RE production via this mechanism is called Dreicer growth.<sup>1</sup> Other primary generation mechanisms are possible during transient periods of strong  $E_\phi/E_D$ , such as during a thermal collapse<sup>4,5</sup> or magnetic reconnection events.<sup>6</sup> However, these mechanisms are not the focus of this work and primary production will be used hereafter to refer exclusively to the Dreicer mechanism.

Unlike the expectation from Eq. (1), relativistic effects cause the drag on the most energetic REs to remain finite. This introduces a second field strength which must be exceeded in order to observe electron runaway. This is the Connor-Hastie field, also known as the “critical” field<sup>7</sup>

$$E_C = \frac{n_e e^3 \ln \Lambda}{4\pi \epsilon_0^2 m_e c^2} \equiv \left( \frac{T_e}{m_e c^2} \right) E_D. \quad (2)$$

Once a population of REs has been excited (by primary generation) to sufficiently high energy, the close collision of a RE with a thermal electron can transfer enough momentum such that both electrons are now REs, yielding exponential growth. This is the secondary generation mechanism (also known as RE avalanche). First proposed using *ad-hoc* models,<sup>8,9</sup> this mechanism was later verified using a relativistic collision operator.<sup>10,11</sup> Though the rate depends on plasma parameters, secondary growth is predicted to occur when  $E_\phi > E_C$ .

Primary growth can become large during a tokamak disruption, where  $E_\phi$  becomes very large and induces hot-tail growth.<sup>12</sup> After the transient primary seed, secondary generation can take over and RE growth continues, resulting in a

RE plateau.<sup>13,14</sup> In the plateau regime, measurement of the parameters important to primary and secondary growth is very challenging. This is due to the large transients present as well as the uncertain impurity profile after high-Z gas or pellets are injected to induce or mitigate the disruption.<sup>15,16</sup>

REs can also be excited by initiating a discharge at very low early density, yielding the slide-away regime.<sup>17–19</sup> The transiently large  $E_\phi$  during discharge formation forces a large fraction of the thermal electrons to run (or “slide”) away and carry much of the plasma current ( $I_p$ ). This regime is characterized by low  $T_e$  and  $E_\phi$ , as well as large periodic bursts in the RE signal thought to be due to the Parail-Pogutse instability,<sup>20</sup> though other instabilities have been proposed.<sup>21</sup> Due to beam instability-induced transients, this regime is also difficult for accurate measurements of RE growth.

A variant of the slide-away regime, here termed the quiescent RE regime, yields REs free of equilibrium or non-thermal transients. This regime is achieved by accessing very low densities during Ohmic flat-top (after discharge formation) while also avoiding error field (EF) penetration by staying above the low-density locked-mode (EF penetration) limit.<sup>22–24</sup> The distinction made from the traditional slide-away regime is that in the quiescent regime early-time slide-aways are suppressed via large early densities. On DIII-D, this is experimentally found to prevent the periodic RE instabilities which otherwise occur.<sup>25</sup> Great care must also be taken to avoid EF penetration as this is experimentally seen to introduce large irregular fluctuations in the RE signal despite the stationary nature of the torn magnetic topology. The quiescent RE regime has been historically accessed on ASDEX<sup>26</sup> and TEXTOR<sup>27–29</sup> though those studies predated more complete theoretical treatments.<sup>10</sup> More recently, this regime was re-visited on TEXTOR to examine RE behavior after the application of various 3-D field structures, though some structures yielded large bursting behavior (possibly due to EF penetration) and thus were no longer quiescent.<sup>30,31</sup>

This paper will use the quiescent RE regime to measure the growth and decay of RE populations and make comparisons with primary and secondary RE generation rates. The RE onset dynamics will be shown to be well captured by Dreicer-only primary theory, with long quiescent growth periods spanning nearly the entire 7 s flat-top characterized across several diagnostics. The effect of gas puffing will then be presented, both on the equilibrium as well as the non-thermal population. It will be shown that the transition from growth to decay occurs not at  $E_\phi = E_C$  as expected by secondary theory, but at  $3 \leq E_\phi/E_C \leq 5$ , and is thus indicative of anomalous RE loss. Previous studies in the post-disruption plateau regime have noted a similar discrepancy in the required  $E_\phi$  which was also attributed to anomalous RE loss.<sup>15,16</sup> This work complements those studies by presenting a similar result without the measurement ambiguities of the plateau regime, though is not presently known if the loss mechanisms are similar in both regimes.

The structure of this paper is as follows. Section II describes the experimental setup and presents equilibrium measurements before and after the re-introduction of gas

puffing. Section III presents measurements of RE onset and relates the onset condition to the primary production rate. Section IV details the dynamics of the growth phase using information from various diagnostics. Section V systematically presents the transition from growth to decay across several dedicated discharges. Section VI characterizes the decay phase, and magnetic fluctuation measurements are presented in Sec. VII. Discussion and concluding remarks are given in Sec. VIII.

## II. DISCHARGE SETUP AND EQUILIBRIUM PROFILES

Figure 1(a) presents the basic plasma parameters of the tokamak discharge, which are unchanged throughout this dataset.  $I_p$  is held at 0.8 MA, which both reduces flux consumption of the Ohmic coil as well as lowers particle confinement supporting  $n_e$  pumpout. Toroidal field ( $B_T$ ) is set to 1.48 T, yielding  $q_{95} = 4.6$ . A relatively high  $q_{95}$  value is used to yield non-disruptive EF penetration events. Internal inductance  $l_i = 1.5$ , indicating that the current profile is peaked and reaches a relaxed state by  $\approx 1.6$  s. All discharges contain low-level sawtooth activity<sup>32</sup> with a period of about 25 ms. The discharge duration is limited in all cases by engineering limits on the Ohmic coil. Note  $B_T$  here is well below the *ad-hoc* limit of  $B_T \geq 2$  T for RE generation,<sup>33</sup> though this is unsurprising since this regime is non-disruptive and further no dimensional engineering parameter can be meaningfully compared across devices without being first non-dimensionalized.

The line-averaged density evolution for typical discharges of the experiment is shown in Fig. 1(b). The initial density is held above  $10^{13} \text{ cm}^{-3}$  which prevents slide-aways during the formation phase. After the formation phase, gas puffing is disabled at 0.8 s and the density is left to pump-out. Significant variations in the pump-out rate are found due to wall conditions. Figure 1(c) illustrates that after some time, RE-generated hard x-rays (HXR) become visible. Gas puffing is then re-introduced near the end of the

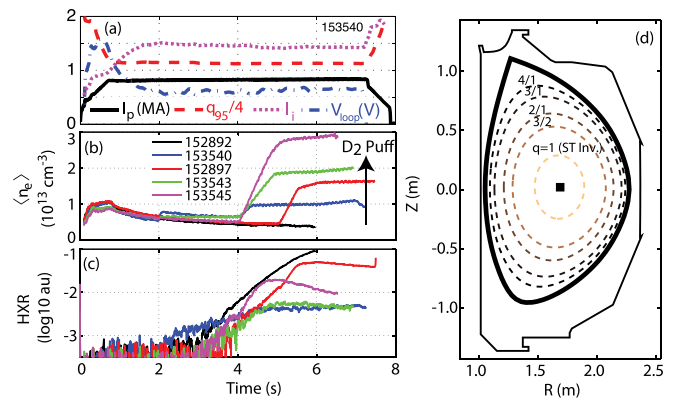


FIG. 1. Description of scenario used to excite runaway electrons in Ohmic flat-top. (a) Long-duration relaxed discharges in which  $I_p = 0.80$  MA,  $B_T = 1.48$  T,  $q_{95} = 4.6$ ,  $l_i = 1.5$ ,  $V_{\text{loop}} = 0.6$  V. (b) Line-averaged density as measured by CO<sub>2</sub> interferometer for a representative sub-set of the discharges of this experiment. (c) HXR signal from a plastic scintillator (Bicron BC-400) used as a proxy for the number of runaways, illustrating growth and decay as density is stepped. (d) Plasma shape including location of rational surfaces. The  $q = 1$  surface is taken to be the sawtooth inversion radius.

discharge, which causes variations in the REs which are the subject of this work. Interpretation of the HXR signals will be further discussed in Sec. IV C.

Such low density regimes on DIII-D are generally inaccessible due to the appearance of low-density EF penetration events. This instability is avoided in this work due to precise correction of the DIII-D intrinsic error field with ex-vessel coils.<sup>34</sup> Data are truncated where EF penetration occurs, as in the black trace of Fig. 1(b) just before 6 s. The discharge scenario is also diverted, as shown in Fig. 1(d), which helps to keep the plasma free of impurities. The plasma is an upper-biased double null configuration corresponding to the  $\nabla B$  drift with a higher L-H power threshold to avoid inadvertent H-mode transitions and consequent density increases. Figure 1(d) also shows the locations of the rational surfaces obtained through EFIT reconstructions constrained by motional Stark effect (MSE) polarimetry measurements.

Excellent equilibrium reconstructions and profile diagnosis of the discharge are possible via the use of 5 ms neutral beam blips. Figure 2 presents the measured profiles for a typical case with (solid) and without (dash) late-time gas puffing. Figures 2(a) and 2(b) show the density evolution and HXR signal with the timing of the diagnostic beam blips clearly visible. Figures 2(c)–2(h) illustrate representative profiles at a few time-slices (indicated by the color code). Gross dependencies are shown with arrows, and data points are included for a representative profile. As the density is reduced due to pump-out [Fig. 2(c)], several changes occur. The carbon impurity density is relatively constant such that a reduction in  $n_e$  causes an increase in  $Z_{\text{eff}}$  and vice-versa [Fig. 2(d)]. This is especially dramatic after the puff, with the final  $Z_{\text{eff}}$  very near to unity. As  $n_e$  drops,  $T_e$  [Fig. 2(e)] increases and  $T_i$  [Fig. 2(f)] decreases. This is due to a decreased electron-ion collision rate and thus decreased energy transfer from the Ohmically heated electrons to the ions. This too is reversed after the puff, with  $T_e/T_i$  going from  $\approx 4 \rightarrow 1.5$ . Interestingly, measurements of toroidal carbon [Fig. 2(g)] and deuterium (not shown) rotation illustrate that gas puffing causes a bifurcation from co-rotation to counter-rotation in the core, while the edge remains co-rotating. This phenomenon is found on other devices,<sup>35</sup> though further discussion is outside the scope of this work. Finally, the current profile [Fig. 2(h)], and thus the low-pressure MHD equilibrium, is stationary both with and without gas puffing.

### III. DREICER ORIGIN OF RUNAWAY ONSET

The condition for detectable onset of the RE population is summarized in Fig. 3. Contrasting the highest density (black) trace in Figs. 3(a) and 3(b), with the subsequent discharges, it is shown that increasing the density by merely 25% is sufficient to reduce the HXR signal by at least 100× and prevent it from rising above the noise floor. Furthermore, it is clear that slight variations in the (uncontrolled) density rampdown rate after 0.8 s yield sizable ( $\gtrsim 1$  s) temporal delays in the appearance of the HXR signal. This extreme sensitivity to onset conditions has the appearance of a criticality condition and was first interpreted as

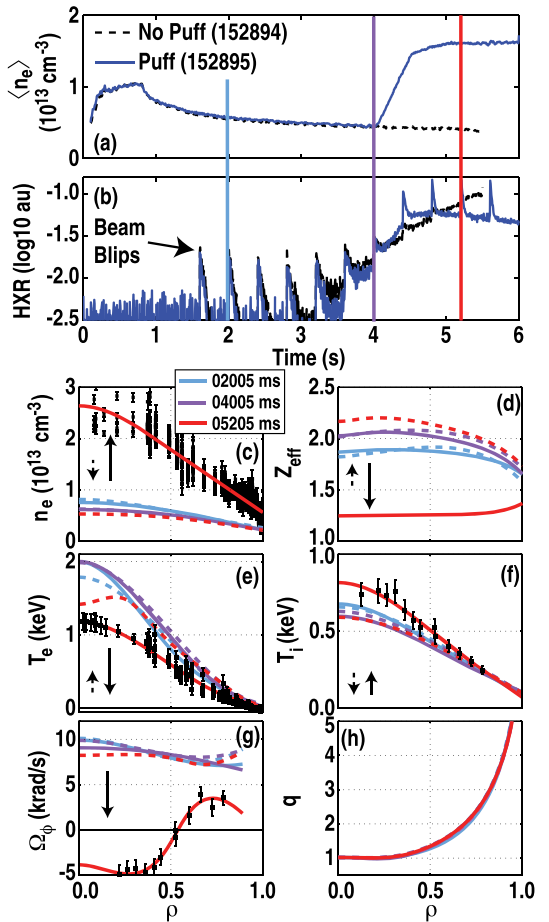


FIG. 2. Profiles for representative discharges with (solid) and without (dash) gas puffing. (a) and (b) illustrate the temporal evolution, with diagnostic beam blips observable on the plastic scintillator. (c)–(h) Profiles as measured by TS, carbon charge-exchange recombination (CER) spectroscopy, and MSE polarimetry for a few time-slices in each discharge. Arrows illustrate rough direction and magnitude of profile changes with and without gas puffing. Data points are only shown for the last time-slice of the puffed discharge, with beam blips yielding fewer CER points than the continuous TS measurement.

a critical density for RE growth. However, the different trajectories of the discharges in Figs. 3(a) and 3(b) suggest that the overall time-history of the discharge must be considered, not simply the density at which the HXR signal is first observed.

This is accomplished via 0-D modeling of primary and secondary RE generation using measured time-traces of  $n_e$ ,  $T_e$ ,  $E_\phi$ , and representative  $Z_{\text{eff}}$  values from beam-blipped discharges. The RE growth is modeled as in Ref. 2, with a simple treatment of the RE generation problem

$$\frac{d(n_{\text{RE}})}{dt} = \underbrace{S_{\text{pri}}}_{\text{primary}} + \underbrace{\gamma_{\text{sec}} n_{\text{RE}}}_{\text{secondary}}. \quad (3)$$

The terms in the above equation are given by

$$S_{\text{pri}} = kn_e \hat{\nu}_{ee} \epsilon_D^{-\frac{3}{16}(1+Z_{\text{eff}})} \exp\left[-\frac{1}{4}\epsilon_D^{-1} - (1+Z_{\text{eff}})^{\frac{1}{2}}\epsilon_D^{-\frac{1}{2}}\right] \\ \times \exp\left(-\frac{T_e}{m_e c^2} \left[\frac{1}{8}\epsilon_D^{-2} + \frac{2}{3}(1+Z_{\text{eff}})^{\frac{1}{2}}\epsilon_D^{-\frac{3}{2}}\right]\right), \quad (4)$$

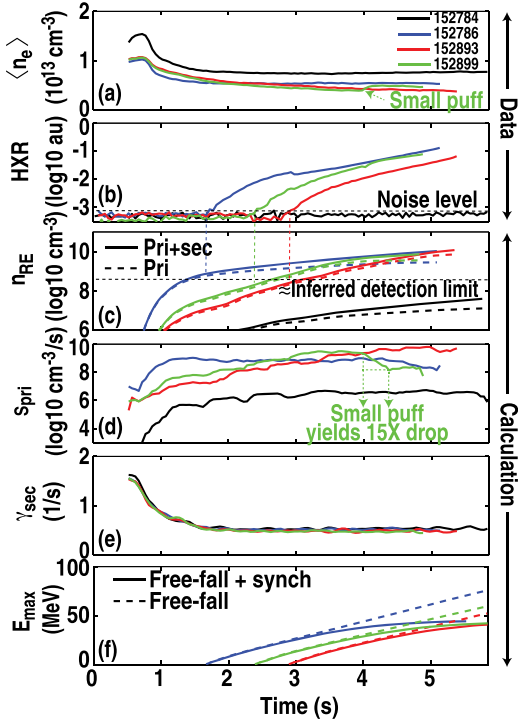


FIG. 3. Comparison of experimental data [(a) and (b)] and calculation of Eqs. (3)–(6) [(c)–(e)] which captures the onset of HXR signals as density is decreased. Note  $V_{\text{loop}}$  evolution is nearly identical for these discharges and is not shown. (f) Maximum achievable RE energy with and without synchrotron losses for a single RE initiated with 1 MeV at the HXR onset time.

$$\gamma_{\text{sec}} = \frac{\epsilon_C - 1}{\tau \ln \Lambda} \sqrt{\frac{\pi \varphi}{3(Z_{\text{eff}} + 5)}}, \quad (5)$$

$$\left[ 1 - \epsilon_C^{-1} + \frac{4\pi(Z_{\text{eff}} - 1)^2}{3\varphi(Z_{\text{eff}} + 5)(\epsilon_C^2 + 4/\varphi^2 - 1)} \right]^{-\frac{1}{2}}, \quad (6)$$

where in the above equations  $\epsilon_{\{D,C\}} \equiv E_{\phi}/E_{\{D,C\}}$  is the normalized electric field,  $k = 0.21 + 0.11Z_{\text{eff}}$  is an order unity correction,<sup>36</sup>  $\varphi = 1 - 1.46(r/R_0)^{\frac{1}{2}} + 1.72(r/R_0)$  is a neoclassical correction factor, and  $\tau = (c/v_{T_e})^3 \hat{v}_{ee}^{-1}$  is the RE collision time. Note that potential sinks of RE populations not included in Eqs. (3)–(6) are considered anomalous, and will be discussed in Secs. VII and VIII.

Due to the well-diagnosed nature of these discharges, all parameters needed to evaluate Eqs. (3)–(6) are known with good accuracy. Furthermore, since the total  $n_{\text{RE}}$  is always small compared to  $n_e$ , the back-reaction of the RE population onto  $E_{\phi}$  can be neglected. Figures 3(c)–3(e) present the calculation of Eqs. (3)–(6) for comparison to the HXR signal. While  $\gamma_{\text{sec}}$  is calculated to be effectively equal across the discharges,  $S_{\text{pri}}$  displays wide variance. The integration of Eq. (3) [Fig. 3(c)] is able to reproduce the temporal delays observed in the experiment. Furthermore, the calculation suggests the HXR signal can only detect  $n_{\text{RE}} > \mathcal{O}(10^{8.5}) \text{ cm}^{-3}$ , though an absolute calibration of the plastic scintillator is left to future work. It should also be noted that the absolute  $n_{\text{RE}}$  level is sensitive to the flux surface chosen for evaluation of  $n_e$  and  $T_e$ , though relative variation across

discharges is insensitive. The calculation also confirms that the slightly higher density discharge never reaches this detection level, though given a much longer time it may have eventually become visible. The appearance of a burst of HXR activity when the higher density case disrupts at 6 s (not shown) also confirms that a small, undetected RE population exists even in the higher density case. The energy gain by a RE in free-fall and including synchrotron losses are also presented Fig. 3(f) (using the formalism found in Ref. 37) illustrating that in this equilibrium the RE energy is limited to about 50 MeV by synchrotron losses. Synchrotron losses are expected to dominate over bremsstrahlung at high energy in the deuterium plasma.<sup>38</sup>

This calculation also indicates that the discharges without gas puffing are generally dominated by primary-sourced runaways. However, even small levels of puffing cause the primary source term ( $S_{\text{pri}}$ ) to weaken exponentially leaving the secondary term ( $\gamma_{\text{sec}}$ ) to dominate the growth. This is exemplified in the 15-fold decrease in  $S_{\text{pri}}$  [Fig. 3(d)] in discharge 152899 at 4 s after a barely perceptible density rise [Fig. 3(a)]. This will be the technique used in Sec. V to separate primary and secondary growth. Finally, while only a subset of discharges is shown, similar agreement with the pre-puff onset phase is found across the dataset. This indicates that the pre-puff RE onset is well captured by the Dreicer growth model, with exponential sensitivity to  $\epsilon_D$  (and thus  $n_e$ ) yielding a false criticality condition.

#### IV. CHARACTERIZATION OF PRIMARY GROWTH PHASE

During the quiescent growth phase (without gas puffing), RE signatures are visible on a number of diagnostics besides the plastic HXR scintillators. Modeling of the expected time-dependent energy distribution is also tractable, and qualitative comparisons to various measurements are presented.

##### A. Fokker-Planck model

To model the energy distribution [ $f(E)$ ] evolution, the 0-D Fokker-Planck solver CODE<sup>39</sup> is used. This model uses a relativistic collision operator valid for small-angle collisions at arbitrary energies. Large-angle collisions, such as those needed for secondary generation, are not treated self-consistently. Dissipation from radiative processes (synchrotron, bremsstrahlung) is not included, and the only particle loss occurs when a particle gains enough energy to leave the simulation velocity-space boundary. The modeling approach is to take time-averaged core parameters of the no-puff discharge type of Fig. 2 and to launch a time-dependent simulation. Figure 4 shows that a high-energy RE tail is gradually excited as a function of time. The time it takes to reach high energy is essentially a free-fall process, similar to the calculation shown in Fig. 3(e). Since  $E_{\phi} \approx 50 \text{ mV/m}$  and the DIII-D major radius is 1.67 m,  $dE/dt \approx 15 \text{ MeV/s}$ , it takes  $\approx 3 \text{ s}$  to reach  $\gamma = 100$ . Although secondary generation is not included in this simulation, it is interesting to note that after sufficient time the slope in  $f(E)$  is very near to the predicted slope of an avalanche distribution, which itself is only weakly sensitive to plasma parameters through the  $\ln \Lambda$  and

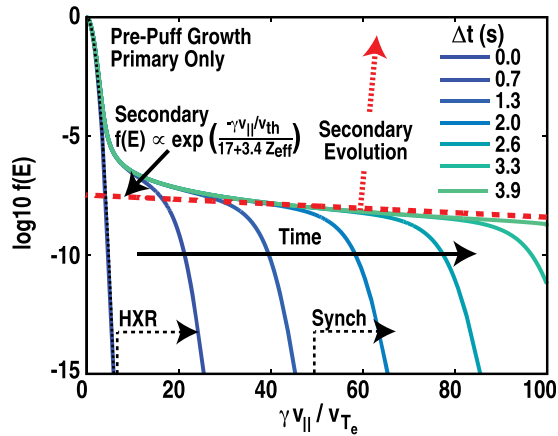


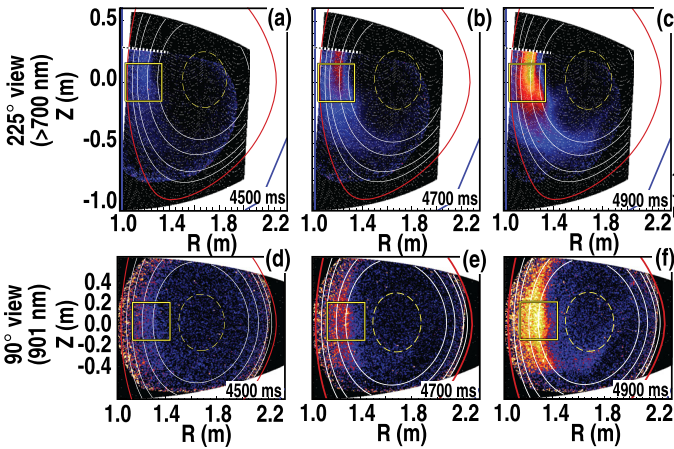
FIG. 4. Normalized energy distribution [ $f(E)$ ] time-dependent modeling excluding secondary generation. No-puff discharge is used, illustrating slide-away of the high energy tail as a function of time after Dreicer growth commences. Dotted lines indicate analytic evaluation of secondary-dominated distribution (with  $Z_{\text{eff}}$  set to 2), as well as evolution direction. Secondary  $f(E)$  maintains constant slope while increasing in number. Approximate detection limits for HXR and SE are also shown.

$Z_{\text{eff}}$  terms.<sup>11</sup> Thus, while these discharges have excited REs via the primary mechanism, their energy distribution (after sufficient time) is found to be a close match to an avalanche-dominated  $f(E)$ .

## B. Synchrotron emission spatial dependence

Despite the small value of  $n_{\text{RE}}/n_e$ , visible synchrotron emission (SE) imaging of the RE population with a fast camera<sup>37</sup> is possible in these discharges, owing to the exceedingly strong dependence of the SE power on the RE energy ( $P \propto \gamma^4$ ). Unlike plateau RE observations, the SE pattern is found to be stationary in these discharges, with the exception of dynamics during and after EF penetration. This supports the conjecture that the RE evolution is well captured by 0-D modeling, as no changes in spatial distribution are observed during RE growth.

While the SE pattern is stationary, it is found to be neither circular nor concentric with the magnetic axis (which is well known from MSE-constrained equilibrium reconstructions). Instead, as shown in Figs. 5(a)–5(c), the SE is characterized by a crescent shape on the high-field side (HFS). This emission shape is qualitatively reproduced



across two toroidal views separated by  $135^\circ$  toroidally, thus, it is thought to be axisymmetric. Mapping to equilibrium flux surfaces on the tangency plane accurately localizes the SE due to the forward-beaming effect. The SE is found to be absent from approximately inside the  $q = 1$  surface and outside the  $q = 3$  surface.

The absence of SE to the HFS of the  $q = 3$  surface is consistent with the RE drift orbits, which are calculated assuming purely axisymmetric fields with the MAFOT code<sup>40</sup> and are shown in Fig. 5(g). Injection at the  $q = 3/2$  HFS extent demonstrates that REs with  $E > 40$  MeV are no longer confined and strike the limiter due to the drift-orbit effect. Using the same calculation, for  $q = \{2, 3, 4\}$ , the maximum energy is  $\{30, 19, 14\}$  MeV. Since the RE must have  $E \geq 25$  MeV to emit visible SE and be detected, the drift orbit near  $q = 3$  effectively sets the SE limiting surface. The absence of SE inside the  $q = 1$  surface is not quantitatively understood, but is conjectured to be due to the perturbations introduced by the sawtooth cycle, which may be deconfining particles in the core of the plasma. The relative absence of SE on the low-field side may be an artifact of the conservation of magnetic moments ( $\mu \propto v_\perp/|B|$ ), with larger  $v_\perp$  and thus larger SE is generated where  $|B|$  is greatest. In summary, the hypothesis put forward is of an annulus of REs outside the  $q = 1$  surface yet inside of the drift-orbit limiter for each RE energy, with the SE weighted to the HFS due to moment conservation. This hypothesis requires confirmation with a synthetic diagnostic of the SE, for which these discharges would be an ideal benchmark. Similar patterns have been reported in certain phases of the traditional (bursty) slide-away regime in some devices,<sup>19</sup> though in contrast other devices report the observation of (lower energy) SE throughout the core.<sup>41,42</sup> It should also be noted that similar shapes have been observed in the plateau RE regime, where no indications of sawtooth activity have been observed.<sup>37</sup>

## C. Growth rate comparison across diagnostics

This study primarily uses a plastic scintillator (polyvinyl-toluene BC-400) detector<sup>43</sup> for detecting HXRs due to its superior signal to noise (S/N) ratio as well as its broad energy sensitivity. Additionally, DIII-D possesses several other diagnostics able to measure the RE population. Figure 6 illustrates a no-puff RE growth phase across the RE diagnostics for

FIG. 5. Visible SE images of RE growth as measured from two different toroidal views illustrating growth at constant shape. (a)–(c) is at  $225^\circ$  and measures the  $>700$  nm range, with white dashed lines indicating view extent. (d) and (e) is at  $90^\circ$  and measures at 901 nm, though vignetting causes the HFS extent to be poorly resolved. Also overlaid are  $q = \{4, 3, 2, 1.5\}$  surfaces (solid white) and sawtooth inversion radius (dash yellow). (g) indicates of the drift orbits for REs launched on the HFS at the  $q = 3/2$  surface and resultant unconfined RE region.

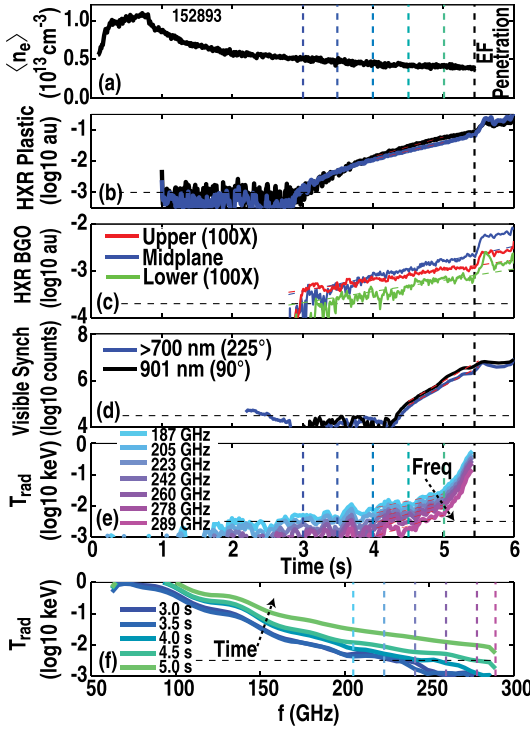


FIG. 6. Measurement of RE growth across several diagnostics while density (a) is dropping. (b) Plastic scintillator, (c) BGO detectors, (d) visible synchrotron, high-frequency ECE in time-domain, (e) and frequency domain (f). Horizontal dashed lines indicate an approximate noise floor for each diagnostic.

which S/N is acceptable. Figure 6(b) demonstrates the equivalence of the growth across two distinct plastic scintillator detectors, both on ports above the midplane and at similar toroidal locations, though at variable distances from the plasma. The relative gain is variable, so the absolute signal level is not comparable. A comparison of the two plastic scintillator growth rates across the entire dataset finds the two to be equivalent to within  $\pm 0.2 \text{ s}^{-1}$ . Figure 6(c) shows the growth across a poloidal array of Bismuth-Germanium-Oxide (BGO) HXR detectors,<sup>44</sup> which roughly measure the same energy range ( $\geq 1 \text{ MeV}$ ) as the plastic scintillator. The gain is  $100\times$  lower on the midplane BGO, yet its signal is comparable to the upper and lower BGO detectors. Thus, the HXR emission is strongest at the machine midplane. To corroborate this, a vertical displacement event (VDE) was triggered. As the plasma moved up the midplane BGO emission decreased while the upper BGO emission increased. This leads to the interpretation that in this regime the HXR signals are not measuring the strike-point loss of REs but instead are measuring bremsstrahlung from REs deflecting on either plasma ions or midplane limiter solid-target ions. The HXR signal is also observed to be linearly proportional to the plasma density, visible for example in Fig. 1(b), thus, deflection from plasma deuterium ions is likely important. This is also consistent with the  $Z_{\text{target}}^2$  scaling of bremsstrahlung radiation, as carbon ( $Z_C = 6$ ) is the dominant impurity and its density is relatively constant at  $n_C \approx 2 \times 10^{11} \text{ cm}^{-3}$ , such that  $n_C Z_C^2 / n_e \approx \mathcal{O}(10^{-1})$ .

Figure 6(d) displays the visible SE integrated counts contained within the squares shown in Fig. 5. Two traces are

plotted, corresponding to the two views shown in Fig. 5. On both views, the signal rises above the noise floor approximately 1.5 s later than the HXR signals. Due to the very strong energy scaling of the SE, REs must reach  $\approx 25 \text{ MeV}$  before they are detected. This delay is roughly consistent with the free-fall time from  $\approx 1 \text{ MeV}$  (the HXR detection threshold) to  $\approx 25 \text{ MeV}$  with an energy free-fall rate of  $15 \text{ MeV/s}$ . As the emission shape is not varying, the observed growth rate is thus a convolution of  $n_{\text{RE}}$  and  $E_{\text{RE}}$ , with a strong  $E_{\text{RE}}$  weighting. The final diagnostic used to detect quiescent RE growth is a fast-scanning Michelson interferometer<sup>45</sup> measuring electron cyclotron emission (ECE) across a wide frequency band, shown in Figs. 6(e) and 6(f) in time and frequency domain, respectively. While numerical calculation of ECE spectra from experimentally constrained RE distribution functions is possible,<sup>46</sup> it is beyond the scope of this work. Presentation of ECE spectra is thus included simply to illustrate the development of a high-frequency tail concurrent with the quiescent growth observed in other diagnostics.

A comparison of growth rates measured from the diagnostics presented in Fig. 6(a) for no-puff discharges is shown in Fig. 7, along with calculated energy sensitivities for SE and HXR diagnostics [Fig. 6(b)]. Also included is a numerical evaluation of  $\gamma_{\text{sec}}$  from Eq. (6), as well as a growth rate fit to the ODE analysis of Eq. (3) [traces as in Fig. 3(c)], both with and without secondary generation. Similar growth rates are found between the ECE, HXR, and either ODE analysis for these similar discharges. Measured growth rates are above those predicted from  $\gamma_{\text{sec}}$ , indicating that primary

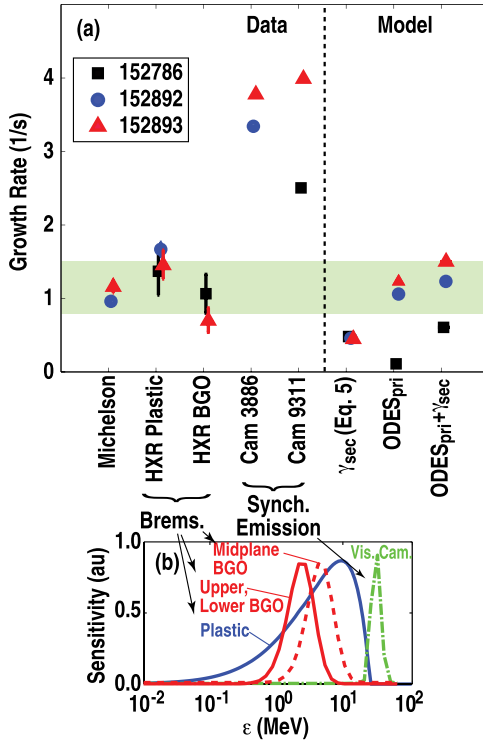


FIG. 7. (a) Comparison of growth rates measured across the diagnostics of Fig. 6 for several no-puff discharges. Also included are theoretical and numerical calculations of the growth rate utilizing measured equilibrium parameters. Energy sensitivity of selected diagnostics is shown in (b).

growth is the important mechanism for these discharges. A notable exception is discharge 152786 [blue trace of Fig. 3(a)]. In this discharge, poorer wall conditions caused the line averaged density to asymptote and primary generation stagnated. Since long-duration exponential HXR growth is still measured, a stronger contribution from secondary generation is inferred. Though most measurements and calculations yield growth rates of  $\approx 1 \text{ s}^{-1}$ , the visible SE is a clear outlier. This is hypothesized to be due to the much greater energy sensitivity ( $P \propto \gamma^4$ ) of the SE, which in conjunction with the evolution of the distribution function to higher energy as calculated in Fig. 4 would lead to a faster effective growth rate. This also suggests that a buildup of the high energy tail is still taking place in these discharges.

The combined analysis of several diagnostics is thus qualitatively consistent with the picture of Fig. 4. A population of REs is growing both in number and maximum energy as a function of time, with a similar growth rate found across diagnostics for which the dominant sensitivity is to RE number as opposed to RE energy.

## V. ANALYSIS OF GROWTH AND DECAY RATES AFTER DEUTERIUM PUFFING

A systematic scan of deuterium gas puffing is undertaken in these discharges. Gas puffing is re-introduced late in the discharge after the primary growth mechanism had built up a measurable population of REs, with example time-traces shown in Figs. 1 and 2. To analyze this dataset, stationary windows within each discharge are isolated. These windows are generally 1–2 s long and found before and after the density rise (gas puff). Within each window, average values and profiles of required equilibrium parameters are defined and the HXR growth rate is also measured and fit. As can be seen in Figs. 1(b) and 1(c), when the density is stationary a well defined HXR growth rate is present.

The gas puffing scan is executed via digital feed-back control of the line-averaged density. This is compared to the core density as measured by the Thomson scattering (TS) system in Fig. 8(a), which will be hereafter presented as the independent parameter. As expected, the core density is slightly larger than the line-averaged value. Note “core” is defined as averaged from  $\rho = 0.0$  to  $0.1$  based on full profile fits such as that of Figs. 2(c) and 2(e), yielding an estimated error of  $\pm 0.2 \times 10^{13} \text{ cm}^{-3}$ . While no SE is imaged from the core of the plasma, this location is chosen for subsequent analysis as it yields the most conservative (largest) estimate of  $E_C$  as  $n_e$  is largest there. Figures 8(b)–8(d) present the dependence of the equilibrium properties across the dataset, complementing the single-discharge profile analysis shown in Fig. 2. As density increases,  $V_{\text{loop}}$  [Fig. 8(b)] increases and  $T_e$  decreases [Fig. 8(c)]. Due to the constant impurity density,  $Z_{\text{eff}}$  decreases upon gas puffing [Fig. 8(d)]. The dataset is also broadly sub-divided based on the size and timing of the gas puff so as to assign a representative  $Z_{\text{eff}}$  value. While a clear distinction occurs between “medium” and “large” puffs ( $\text{core } n_e > 2 \times 10^{13} \text{ cm}^{-3}$ ), the distinction between “small” and “medium” is weaker and also includes a difference in puff timing. Note that a case with weak gas puffing

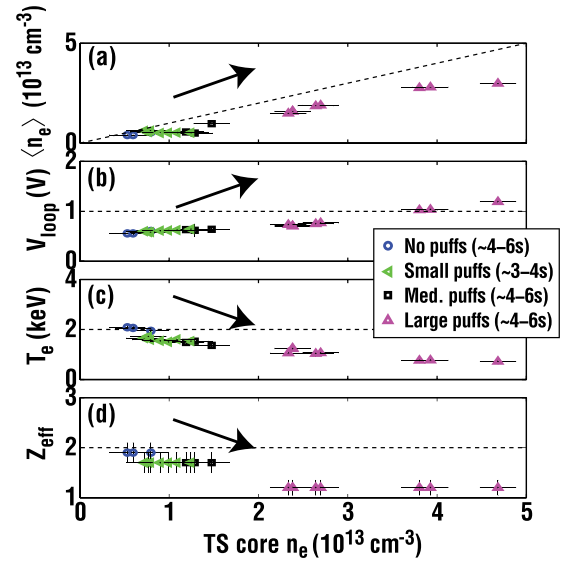


FIG. 8. Variation of equilibrium parameters as gas puffing is re-introduced. (a) Line-averaged density, (b) loop voltage, (c) electron temperature, (d) effective ion charge.

can be equivalent to a no-puff case if wall conditions are not favorable and out-gassing is high.

The equilibrium parameters measured in the dataset are mapped to the relevant RE growth terms according to Eqs. (2), (4), and (6) and this is presented in Fig. 9. As discussed in Secs. III and IV, Fig. 9(a) shows that primary generation rates are found to be potentially measurable [conservatively,  $S_{\text{pri}} \gtrsim (10^5) \text{ cm}^{-3}/\text{s}$ ] for very weak levels of gas puffing as well was for no gas puffing at all. However, above a certain density ( $n_e \gtrsim 10^{13} \text{ cm}^{-3}$ ), the primary generation mechanism is completely suppressed. This is confirmed in the inset,

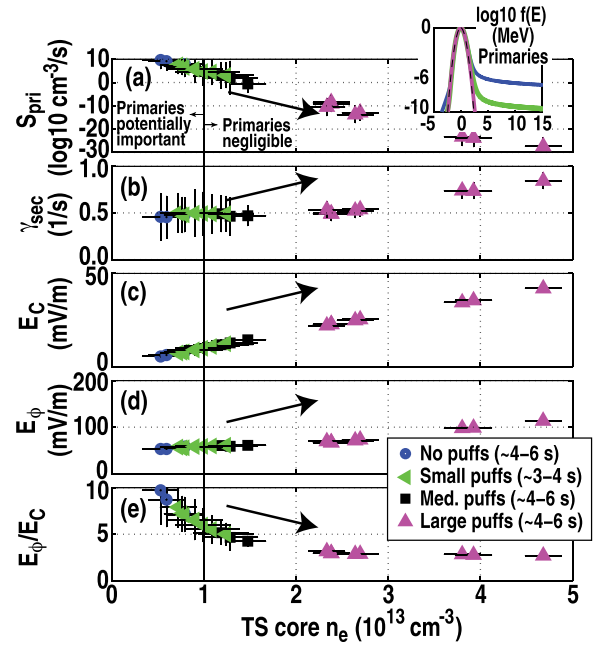


FIG. 9. Dependence of (a) primary ( $S_{\text{pri}}$ ) and (b) secondary ( $\gamma_{\text{HXR}}$ ) calculated growth rates as gas puffing is stepped. Critical electric field (c), toroidal electric field (d), and their ratio (e) are also shown. Inset illustrates time-independent CODE simulation showing greatly reduced population of primaries once modest gas puffing is re-introduced.

which shows CODE calculated steady-state energy spectra for cases of no, small, and large puffs, respectively. This can also be seen in the time-traces of Fig. 3, where the barely perceptible density step of discharge 152899 at 4.0 s yielded a  $15\times$  reduction in  $S_{\text{pri}}$ . Interestingly,  $\gamma_{\text{sec}}$  is predicted to increase [Fig. 9(b)] as gas is puffed. This is despite the increase in  $E_C$  [Fig. 9(c)] and is attributed to both the increase in  $E_\phi$  [Fig. 9(d)] as well as to the e-e collision time ( $\tau \propto \hat{\nu}_{ee}^{-1}$ ) dependence of  $\gamma_{\text{sec}}$ . Though  $E_C$  and  $E_\phi$  both increase, the larger relative increase in  $E_C$  causes  $E_\phi/E_C$  to still decrease [Fig. 9(e)].

Measured HXR growth rates ( $\gamma_{\text{HXR}}$ ) are presented against the relevant dependencies in Fig. 10. To isolate the dataset from contributions from primary growth, only the cases for which  $S_{\text{pri}}$  is negligible [ $S_{\text{pri}} < (10^5) \text{ cm}^{-3}/\text{s}$ ] are kept. Despite this reduction, a transition from HXR growth to decay is still seen as density is increased. It is notable that there are cases for which  $\gamma_{\text{HXR}}$  is still positive despite the elimination of the primary source term, indicating that secondary production is occurring in these discharges.<sup>27</sup> However, the increase in density [Fig. 10(a)] is evidently able to overcome the increase in  $E_\phi$  [Fig. 10(b)] as  $\gamma_{\text{HXR}}$  becomes negative. Cast in terms of  $E_\phi/E_C$ , a transition from growth to decay is found at approximately  $3 \leq E_\phi/E_C \leq 5$ . This is in contrast to the predicted dependency of  $\gamma_{\text{sec}}$  [Eq. (6)], which clearly defines the transition at  $E_\phi = E_C$ . The same information is also shown in Fig. 10(d) as a 2-D map overlain with lines of constant  $E_\phi/E_C$ .

A direct comparison of  $\gamma_{\text{HXR}}$  to the theoretical  $\gamma_{\text{sec}}$  of Eq. (6) is shown in Fig. 11(a). The data points for which primary generation are potentially important have larger growth rates than predicted by secondary theory. While agreement is good for small gas puffs (with  $E_\phi/E_C \gg 1$ ), as puffing is increased ( $E_\phi/E_C$  decreased) agreement is lost. In fact, the observed dependence is found to scale in the wrong direction, with  $\gamma_{\text{sec}}$  increasing while  $\gamma_{\text{HXR}}$  decreases and crosses

zero. Better agreement is found if the  $(\epsilon_C - 1)$  term in Eq. (6) is replaced with  $(\epsilon_C - 4)$ , as suggested by the zero crossing in Fig. 10(c). Assuming an *ad-hoc* anomalous loss time ( $\tau_L$ ) such that  $\gamma_{\text{HXR}} = \gamma_{\text{sec}} - \tau_L^{-1}$  allows an evaluation of the  $\tau_L$  needed to bring experiment and theory into agreement, as shown in Fig. 11(b). The required  $\tau_L$  is in fact not constant, but varies strongly (and linearly) across the scan. Possible reasons for this discrepancy are discussed in Sec. VIII.

## VI. CHARACTERIZATION OF DECAY PHASE

To leave enough time for profile equilibration, gas puffing is introduced 1–2 s before the end of the discharge. This yields RE populations lower in number and maximum energy than cases without gas puffing. Furthermore, gas puffing itself degrades wall conditions, which reduces density pump-out on subsequent shots and further weakens RE population levels. Thus, in the absence of a dedicated series of discharges separated by several clean-up pulses, post-puff RE decay characterization suffers from poorer signal/noise when compared to growth characterization. Nonetheless, qualitative interpretation is still possible and is presented.

### A. Fokker-Plank model

Figure 12 illustrates the expected evolution from the primary-generated distribution function of Fig. 4 after the gas puff has been applied. Specifically, the parameters from the puffed discharge of Fig. 2 are used in the CODE Fokker-Planck simulation using as the initial condition the  $f(E)$  found at steady-state in Fig. 4. Without secondary generation [Fig. 12(a)], the  $f(E)$  slowly collapses as the REs are continually accelerated to high energy but are no longer replaced at low energy by new primaries, inverting  $f(E)$  as the high energy tail is ejected. With secondaries included [Fig. 12(b)], the high-energy tail continues to increase. Note that

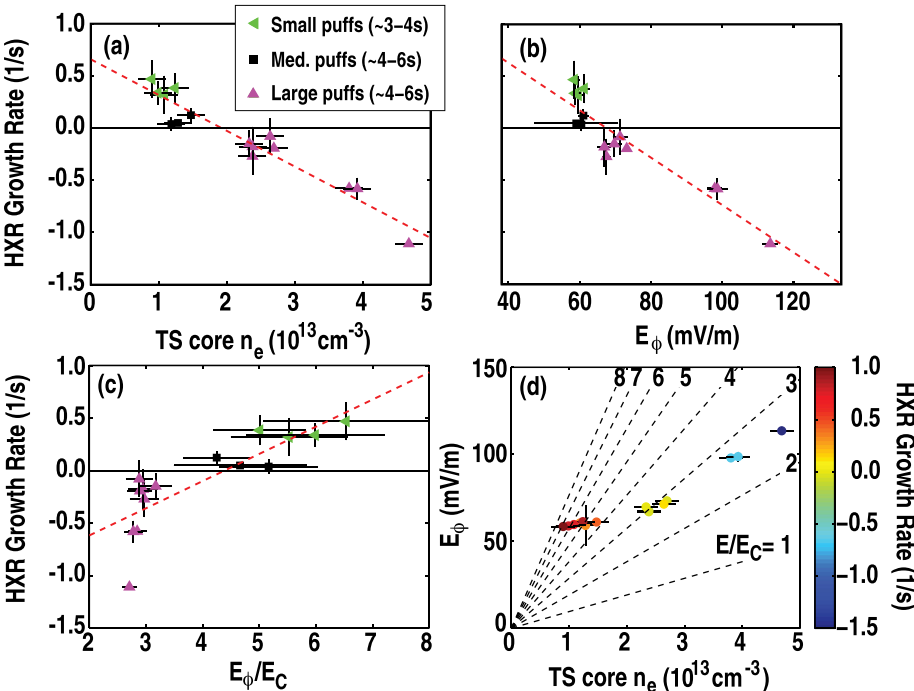
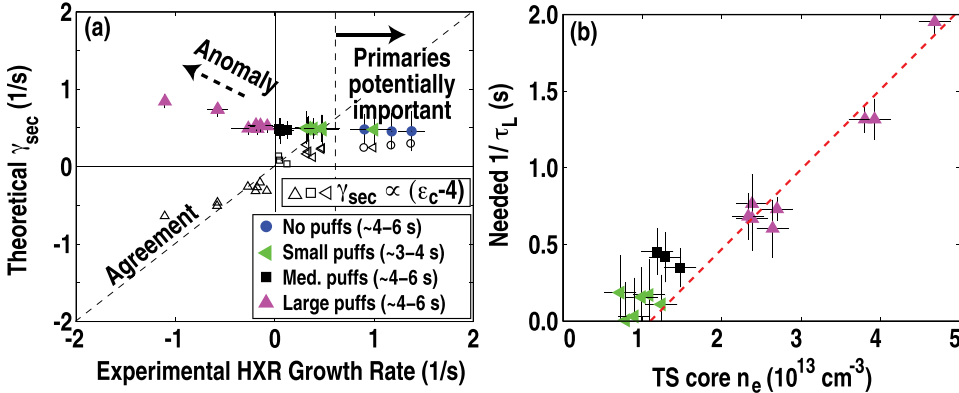


FIG. 10. Comparison of HXR growth rate vs dataset parameters (a)  $n_e$ , (b)  $E_\phi$ , (c)  $E/E_C$ , and (d) composite. Points for which primary generation is potentially important [ $S_{\text{pri}} > \mathcal{O}(10^5) \text{ cm}^{-3}/\text{s}$ ] have been omitted.



secondary generation is not treated self-consistently in the simulation,<sup>39</sup> with the dashed line in (b) indicating the selected secondary birth energy.

## B. Synchrotron emission and decay rate comparison

Synchrotron emission for a discharge with similar density evolution to the puffed discharge of Fig. 2 is shown in Fig. 13. After the puff, a clear transition to decay of both the HXR [Fig. 13(b)] and SE [Fig. 13(c)] signal is seen. Analysis of the SE images immediately following the puff [Figs. 13(d)–13(f)] indicates that the SE decay occurs at constant shape, and furthermore that the shape found in the growth phase (Fig. 5) is unchanged upon gas addition. As with the HXR signals, a prompt increase in the SE is observed concurrent with gas addition. This is due to modest contamination of the camera SE image with increased visible

bremsstrahlung (VB) at higher density which yields a signal increase across the entire plasma cross section. Images presented in Figs. 13(d) and 13(e) are baselined using the image prior to QRE growth (3.5 s), with VB contamination present at the ≈25 % level, visible as the volumetric background emission (blue).

Figure 14 shows a similar growth to decay transition on the ECE emission. Unlike the HXR and SE, the ECE signal is free of direct density dependence and thus a direct identification of the turnover density is possible without the need to apply the window analysis presented in Sec. V. The transition from ECE growth to decay occurs when the line-averaged density is  $(0.9 \pm 0.1) \times 10^{13} \text{ cm}^{-3}$  and core density is  $(1.3 \pm 0.1) \times 10^{13} \text{ cm}^{-3}$ . This is near, but slightly below the zero crossing inferred from Fig. 10(a). The gap in the ECE data at the turning point is due to the appearance of large bursts<sup>47</sup> in the ECE detectors concurrent with the sawtooth crash that temporarily overwhelm the scanning

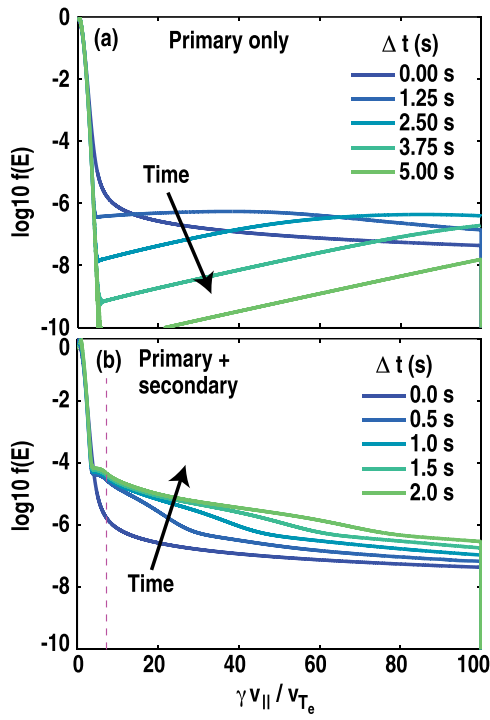


FIG. 12. Time-dependent energy distribution [ $f(E)$ ] modeling of the post-puff equilibrium presented in Fig. 2, using as initial condition the steady-state  $f(E)$  of the no-puff equilibrium. (a) Puffing ceases primary generation causing a collapse of the high-energy tail. (b) Inclusion of a secondary source allows  $f(E)$  to continue to grow.

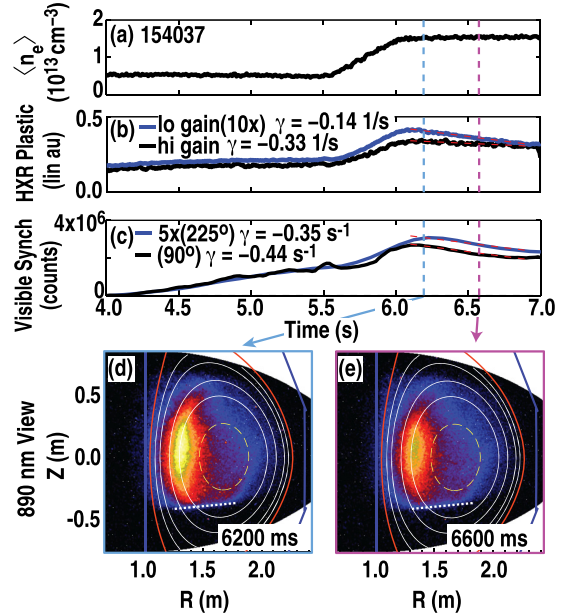


FIG. 13. Growth and decay of HXRs and SE for a puffed discharge with similar density evolution to Fig. 2. As density (a) is increased, the growth of the HXR (b) and SE (c) signal is arrested and decays. Note linear scale is used to highlight the decay phase. (d) and (e) show SE images in the decay phase, illustrating SE decrease at constant shape. The SE lower extent is limited by the field of view (white dashed line).

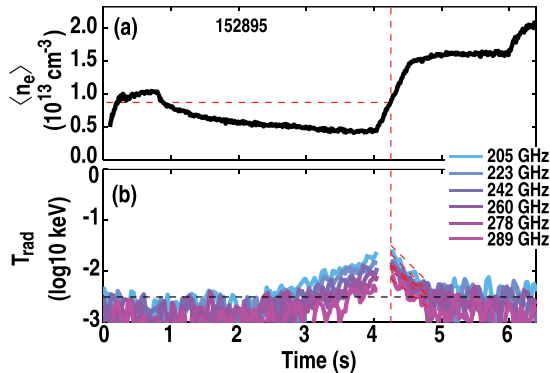


FIG. 14. Growth and decay of high-frequency ECE signal for the puffed discharge whose profiles were shown in Fig. 2. As density (a) is increased, the growth of the ECE signal (b) is arrested and begins to decay and is below the noise floor shortly after density reaches a new flat-top.

interferometer. The burst is speculated to be itself related to the rotation reversal occurring at the same time.

Fitted growth rates to the discharges shown in Figs. 13 and 14 are presented in Table I. Errors are taken to be the variation between redundant measurements as multiple detectors exist for each emission band. Interestingly, the ECE decay rate is in much greater disagreement with the HXR, while the SE decay is similar to the HXR. This is in contrast to what was found in the growth analysis of Sec. IV and suggests that the f(E) distribution is again not changing self-similarly in the decay phase. It is not possible from the present measurements, however, to experimentally constrain the 0-D modeling presented in Fig. 12, although the decay of the SE indicates that the highest energy REs are indeed decaying, unlike Fig. 12(b). Also note that disagreement in the HXR growth rate, despite being large in the relative sense, is comparable with the scatter found across the dataset, as shown in Fig. 10.

## VII. DIRECT MEASUREMENT OF INTERNAL MAGNETIC FLUCTUATIONS

RE loss can potentially result from broad band (turbulent) fluctuations.<sup>48–51</sup> Since runaways are largely collisionless, the runaway orbit deviations (and thus eventual loss) must be dominantly induced by fluctuations of the magnetic field (as opposed to temperature or density). Although previous work has used external Mirnov coils to estimate magnetic fluctuation ( $\delta B$ ) levels inside the plasma,<sup>33</sup> no direct measurement has yet been presented.

A millimeter-wave polarimeter is utilized to make this measurement for a subset of the discharges presented in this work.<sup>52</sup> The polarimeter measures changes in 288 GHz

TABLE I. Comparison of decay rates at  $\langle n_e \rangle = 1.5 \times 10^{13} \text{ cm}^{-3}$  from signals shown in Figs. 13 and 14.

| Shot   | Growth rate ( $\text{s}^{-1}$ ) |                |                  |
|--------|---------------------------------|----------------|------------------|
|        | HXR                             | ECE            | SE               |
| 152895 | $-0.4 \pm 0.1$                  | $-2.0 \pm 0.5$ | N/A              |
| 154037 | $-0.2 \pm 0.1$                  | N/A            | $-0.40 \pm 0.05$ |

electromagnetic wave polarization (with respect to a reference) as the wave propagates from the outboard midplane through the magnetized plasma and retro-reflects on the center-post back to a co-located detector. Polarization changes are induced by either the Faraday Rotation (FR) effect (sensitive to density and magnetic fields parallel to the beam) or by the Cotton-Mouton (CM) effect (sensitive to magnetic fields perpendicular to the beam). Modeling of both effects for the  $n_e$  and  $B_0$  equilibrium profiles presented in Sec. II indicates that the FR effect dominates in the low-density RE growth phase presented in Sec. IV. Furthermore, the close alignment of the viewing chord height with the magnetic axis allows separation of the contributions to the total FR from density fluctuations ( $\delta n_e$ ) as this effect is weighted by the equilibrium  $B_R$  which averages to near zero across the magnetic axis.<sup>53</sup> Unfortunately, for the higher density discharges presented in Sec. VI, the CM effect can become large and no clean separation of  $\delta B$  and  $\delta n_e$  is possible.

Polarimeter  $\delta B$  measurements are presented in Fig. 15 for the discharges and time-slices of Fig. 2. Fluctuation strength is normalized to the toroidal field at the magnetic axis ( $B_0 \equiv 1.48 \text{ T}$ ), and the fluctuation level prior to discharge initiation is included as a noise floor. Integrated over the frequency range accessible to the instrument (1–95 kHz), the total fluctuation strength is measured to be  $(\delta B/B_0) \approx 1 \times 10^{-4}$ , which for these plasmas  $\approx 1 \text{ G}$ . The simple Rechester-Rosenbluth<sup>54</sup> relationship ( $D_{RR} = \pi q v_{||} R (\delta B/B_0)^2$ , where  $q$  is the local safety factor and  $R$  is the major radius) can be thought of as an upper bound as finite Larmor radius and magnetic drift velocity effects are not included, causing the true  $D$  to decrease with RE energy ( $D = D_{RR} G(p)$ , where  $G(p)$  is a reduction factor at RE momentum  $p$ ). Indeed, for the parameters of this equilibrium  $D_{RR} \approx \mathcal{O}(10^1) \text{ m}^2/\text{s}$  is computed—a large value. Comparison to a simple 1-D radial diffusion equation requires  $D > \gamma_{RE} (a/2.4)^2 \approx \mathcal{O}(10^{-1}) \text{ m}^2/\text{s}$  (where  $a$  is the minor radius), thus, these fluctuations could potentially affect RE diffusion, depending on the reduction of  $D$  from  $D_{RR}$  due to the aforementioned corrections, which in turn depend sensitively on the fluctuation structure.<sup>55</sup> Numerical

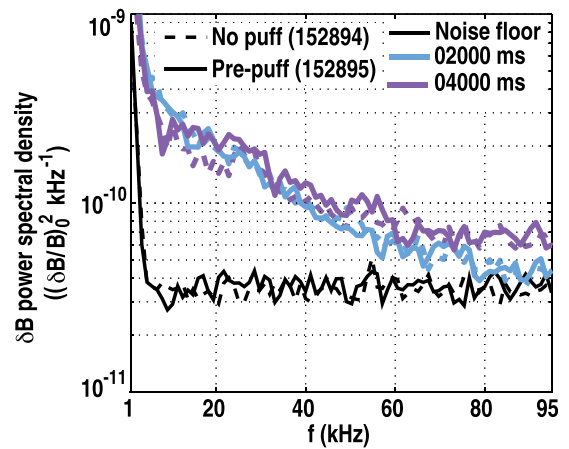


FIG. 15. Density-weighted magnetic fluctuation data as measured by a millimeter-wave polarimeter<sup>52</sup> for the discharges whose profiles were shown in Fig. 2. Also included is the apparent fluctuation measurement prior to discharge initiation, here included as an instrumental noise floor.

calculations in the admittedly different post-disruption regime have quoted<sup>4,49</sup> required fluctuation levels of  $(\delta B/B_0) \approx \mathcal{O}(10^{-3})$  to suppress RE avalanche, a level moderately above the present measurement. It is left to future work to reconcile these measurements with computational modeling varying the spatial structure of the measured  $\delta B$ .

Note that while no  $\delta B$  measurement is made in conditions corresponding to RE decay due to the CM effect, it is speculated that the fluctuations in the post-puff discharges will not have changed appreciably from the present measurements. It should also be noted that fluctuations below 1 kHz are dominated by electrical line noise, and as such coherent fluctuations from the sawtooth cycle (with frequency  $\approx 40$  Hz) are not well known. Note also that no spatial information is available as the fluctuation measurement is line-averaged.

## VIII. DISCUSSION

This work has illustrated a transition from RE growth to decay as deuterium gas puffing (density steps) was re-introduced into quiescent slide-away regime discharges. The transition was not found at  $E_\phi = E_C$  as expected by avalanche growth theory, but instead at  $3 \leq E_\phi/E_C \leq 5$ . Possible sources of discrepancy are now discussed.

These experiments use a RE population born via the Dreicer mechanism to make statements about secondary growth and decay. For this to be valid, the energy distribution [ $f(E)$ ] of a Dreicer-seeded RE population must be similar to a secondary dominated population or alternatively the secondary source rate must be insensitive to the  $f(E)$  distribution. Calculations indicate that for this experiment in fact both conditions are satisfied. Figure 4 shows that while the early  $f(E)$  distribution may not approximate a secondary  $f(E)$ , after a few seconds the slope in the  $f(E)$  distribution is nearly identical to a secondary distribution and it extends to equally high energy. This is speculated to occur because both primary and secondary generation yield REs at low energy ( $< 2$  MeV), leaving the  $f(E)$  slope at high energy to be dominated by processes common to both mechanisms. Though likely a smaller contribution, secondary production will also still occur throughout the primary growth phase (pre-puff) and further act to smooth any  $f(E)$  discrepancies. Computation has also shown<sup>11</sup> that the secondary source (and thus  $\gamma_{sec}$ ) is very insensitive to the  $f(E)$  distribution of the original REs, with delta-function energy distributions at  $\{2, 5, 20\}$  MeV found to yield the same growth rate (to within  $\approx 20\%$ ) of a well-developed secondary  $f(E)$ . It is suspected that the scatter in the data-points shown in Section V may originate from the somewhat different  $f(E)$  spectra present prior to gas puffing, which in turn originate from different primary growth onset times due to variable wall conditions.

Figure 11(b) indicates a loss term could be able to account for the observed discrepancies between experimental and calculated growth rates. A guaranteed source of losses in these experiments is shown in Fig. 5(g). Due to the relatively modest  $I_p$  and  $B_T$ , RE drift orbits become greatly shifted from the magnetic flux surfaces after they reach  $\approx 30$  MeV. REs at sufficiently large energy and minor radius are thus no longer confined and strike a limiting surface. Furthermore,

this calculation has only used axisymmetric fields, and any residual error fields could potentially lead to RE orbit deflections and thus loss at lower energy or smaller minor radius.<sup>56</sup> Thus, if the RE population is found away from the core as suggested by the visible SE images, REs cannot gain energy indefinitely and will eventually be lost. As  $E_\phi > E_C$  across this entire dataset, REs could continue to gain energy and become lost in growth and decay phases alike.

Aside from the loss of REs due to the drift orbit effect, a diffusive loss of REs can occur due to magnetic fluctuations ( $\delta B$ ) as was explored in Sec. VII. Measurements indicate this effect could be appreciable in these plasmas, depending on the detailed structure of the magnetic fluctuations (such as their poloidal location and radial correlation length). Note however that theoretical work has shown that as the effective  $D$  decreases with RE energy, a transition from RE growth to decay cannot be produced as  $\delta B$  increases, though the avalanche could be slowed.<sup>49</sup> Numerical experiments of these losses should be tractable in a computational code such as ARENA,<sup>49</sup> CQL-3D,<sup>11</sup> or NIMROD,<sup>57</sup> coupled with appropriate synthetic diagnostics. This is left to future work. Further experimental investigation of these loss mechanisms is possible by repeating the gas puffing scan presented herein with different equilibrium shaping,  $I_p$ , and/or  $B_T$  levels, which would strongly affect the drift orbits, magnetic fluctuation levels and associated transport,<sup>41</sup> and also the sawtooth character.

## IX. CONCLUSION

This work has presented the first detailed study of RE growth and decay in the quiescent RE regime, which is free from transients, MHD modes, beam instabilities, and other measurement difficulties characterizing the RE regimes traditionally studied. Low density access during Ohmic flat-top excites a primary RE population which builds over several seconds. The growth of the RE population is visible across several diagnostics each sensitive to a different energy range. Introduction of gas puffing late in the discharge is found to transition the observed RE signals from growth to decay, despite the maintenance of  $E_\phi > E_C$  throughout the dataset. Some loss mechanisms are suggested, with further progress possible with more detailed computational modeling of the observed phenomena.

While these observations could potentially have beneficial implications to post-disruption REs growth, they must first be well understood before any projections to the post-disruption regime are made. As such, this result cannot yet be used to infer any reduced density threshold for RE suppression in the post-disruption regime. However, if the anomalous loss mechanisms are common to both regimes, understanding of quiescent RE loss could yield greater confidence (and perhaps new insights) in the modeling of post-disruption RE physics in future devices.

## ACKNOWLEDGMENTS

This work was supported by the U.S. Department of Energy under DE-FG02-99ER54527, DE-AC05-06OR23100, DE-FC02-04ER54698, DE-FG02-07ER54917,

DE-FG02-08ER54984, DE-FG01-08ER54984, DE-FG03-97ER54415, DE-AC05-00OR22725, and SC-G903402. The authors would like to thank D. Eldon for Thomson scattering calibrations; R. J. La Haye, D. C. Pace, and E. J. Strait for assistance with scenario development; V. A. Izzo for useful discussions; W. W. Heidbrink for diagnostic support; and M. Landreman for sharing the CODE program for use by the authors.

- <sup>1</sup>H. Dreicer, *Phys. Rev.* **115**, 238 (1959).
- <sup>2</sup>P. Helander, L.-G. Eriksson, and F. Andersson, *Plasma Phys. Controlled Fusion* **44**, B247 (2002).
- <sup>3</sup>T. C. Hender, J. C. Wesley, J. M. Bialek, A. Bondeson, A. H. Boozer, R. J. Buttery, A. M. Garofalo, T. P. Goodman, R. S. Granetz, Y. Gribov, O. Gruber, M. P. Gryaznevich, G. Giruzzi, S. Günter, N. Hayashi, P. Helander, C. C. Hegna, D. F. Howell, D. A. Humphreys, G. T. A. Huysmans, A. W. Hyatt, A. Isayama, S. C. Jardin, Y. Kawano, A. G. Kellman, C. E. Kessel, H. R. Koslowski, R. J. La Haye, E. Lazzaro, Y. Q. Liu, V. Lukash, J. Manickam, S. Medvedev, V. Mertens, S. V. Mirnov, Y. Naka-mura, G. A. Navratil, M. Okabayashi, T. Ozeki, R. Paccagnella, G. Pautasso, F. Porcelli, V. D. Pustovitov, V. Riccardo, M. Sato, O. Sauter, M. J. Schaffer, M. Shimada, P. Sonato, E. J. Strait, M. Sugihara, M. Takechi, A. D. Turnbull, E. Westerhof, D. G. Whyte, R. Yoshino, H. Zohm, and ITPA MHD Disruption and Magnetic Control Topical Group, *Nucl. Fusion* **47**, S128 (2007).
- <sup>4</sup>R. W. Harvey, V. S. Chan, S. C. Chiu, T. E. Evans, M. N. Rosenbluth, and D. G. Whyte, *Phys. Plasmas* **7**, 4590 (2000).
- <sup>5</sup>P. Helander, H. Smith, T. Fulop, and L.-G. Eriksson, *Phys. Plasmas* **11**, 5704 (2004).
- <sup>6</sup>E. G. Zweibel and M. Yamada, *Annu. Rev. Astron. Astrophys.* **47**, 291 (2009).
- <sup>7</sup>J. W. Connor and R. J. Hastie, *Nucl. Fusion* **15**, 415 (1975).
- <sup>8</sup>N. T. Besedin and I. M. Pankratov, *Nucl. Fusion* **26**, 807 (1986).
- <sup>9</sup>R. J. Jayakumar, H. H. Fleischmann, and S. J. Zweben, *Phys. Lett. A* **172**, 447 (1993).
- <sup>10</sup>M. N. Rosenbluth and S. V. Putvinski, *Nucl. Fusion* **37**, 1355 (1997).
- <sup>11</sup>S. C. Chiu, M. N. Rosenbluth, R. W. Harvey, and V. S. Chan, *Nucl. Fusion* **38**, 1711 (1998).
- <sup>12</sup>L.-G. Eriksson, P. Helander, F. Andersson, D. Anderson, and M. Lisak, *Phys. Rev. Lett.* **92**, 205004 (2004).
- <sup>13</sup>R. D. Gill, *Nucl. Fusion* **33**, 1613 (1993).
- <sup>14</sup>N. W. Eidiets, N. Commaux, E. M. Hollmann, D. A. Humphreys, T. C. Jernigan, R. A. Moyer, E. J. Strait, M. A. Van Zeeland, J. C. Wesley, and J. H. Yu, *Phys. Plasmas* **19**, 056109 (2012).
- <sup>15</sup>E. M. Hollmann, P. B. Parks, D. A. Humphreys, N. H. Brooks, N. Commaux, N. W. Eidiets, T. E. Evans, R. C. Isler, A. N. James, T. C. Jernigan, J. Munoz, E. J. Strait, C. Tsui, J. C. Wesley, and J. H. Yu, *Nucl. Fusion* **51**, 103026 (2011).
- <sup>16</sup>E. M. Hollmann, M. E. Austin, J. A. Boedo, N. H. Brooks, N. Commaux, N. W. Eidiets, D. A. Humphreys, V. A. Izzo, A. N. James, T. C. Jernigan, A. Loarte, J. Martin-Solis, R. A. Moyer, J. M. Muñoz Burgos, P. B. Parks, D. L. Rudakov, E. J. Strait, C. Tsui, M. A. Van Zeeland, J. C. Wesley, and J. H. Yu, *Nucl. Fusion* **53**, 083004 (2013).
- <sup>17</sup>V. S. Vlasenkov, V. M. Leonov, V. G. Merezhkin, and V. S. Mukhovatov, *Nucl. Fusion* **13**, 509 (1973).
- <sup>18</sup>H. Knoepfel and D. A. Spong, *Nucl. Fusion* **19**, 785 (1979).
- <sup>19</sup>R. J. Zhou, L. Q. Hu, E. Z. Li, M. Xu, G. Q. Zhong, L. Q. Xu, S. Y. Lin, and J. Z. Zhang, *Plasma Phys. Controlled Fusion* **55**, 055006 (2013).
- <sup>20</sup>V. V. Parail and O. P. Pogutse, *Nucl. Fusion* **18**, 303 (1978).
- <sup>21</sup>T. Fülöp, G. Pokol, P. Helander, and M. Lisak, *Phys. Plasmas* **13**, 062506 (2006).
- <sup>22</sup>R. Fitzpatrick, *Nucl. Fusion* **33**, 1049 (1993).
- <sup>23</sup>R. Fitzpatrick, *Plasma Phys. Controlled Fusion* **54**, 094002 (2012).
- <sup>24</sup>R. J. Buttery, A. H. Boozer, Y. Q. Liu, J.-K. Park, N. M. Ferraro, V. Amoskov, Y. Gribov, R. J. La Haye, E. Lamzin, J. E. Menard, M. J. Schaffer, and E. J. Strait, *Phys. Plasmas* **19**, 056111 (2012).
- <sup>25</sup>J. T. Scoville and R. J. La Haye, *Nucl. Fusion* **43**, 250 (2003).
- <sup>26</sup>G. Fussmann, D. Campbell, A. Eberhagen, W. Engelhardt, F. Karger, M. Keilhacker, O. Kluber, K. Lackner, S. Sesnic, F. Wagner, K. Behringer, O. Gehre, J. Gernhardt, E. Glock, G. Haas, M. Kornherr, G. Lisitano, H. M. Mayer, D. Meisel, B. Muller, H. Murmann, H. Niedermeyer, H. Rapp, N. Ruhs, F. Schneider, G. Siller, and K. Steuer, *Phys. Rev. Lett.* **47**, 1004 (1981).
- <sup>27</sup>R. Jaspers, K. H. Finken, G. Mank, F. Hoenen, J. A. Boedo, N. J. Lopes Cardozo, and F. C. Schuller, *Nucl. Fusion* **33**, 1775 (1993).
- <sup>28</sup>R. Jaspers, N. Cardozo, and K. H. Finken, *Phys. Rev. Lett.* **72**, 4093 (1994).
- <sup>29</sup>M. Pankratov, R. Jaspers, and K. H. Finken, *Nucl. Fusion* **38**, 279 (1998).
- <sup>30</sup>K. H. Finken, S. S. Abdullaev, M. W. Jakubowski, R. Jaspers, M. Lehnen, and O. Zimmermann, *Nucl. Fusion* **46**, S139 (2006).
- <sup>31</sup>K. H. Finken, S. S. Abdullaev, M. W. Jakubowski, R. Jaspers, M. Lehnen, R. Schlickeiser, K. H. Spatschek, A. Wingen, R. Wolf, and TEXTOR Team, *Nucl. Fusion* **47**, 91 (2007).
- <sup>32</sup>R. J. Hastie, *Astrophys. Space Sci.* **256**, 177 (1997).
- <sup>33</sup>L. Zeng, H. R. Koslowski, Y. Liang, A. Lvovskyi, M. Lehnen, D. Nicolai, J. Pearson, M. Rack, H. Jaegers, K. H. Finken, K. Wongrach, and Y. Xu, *Phys. Rev. Lett.* **110**, 235003 (2013).
- <sup>34</sup>C. Paz-Soldan, R. J. Buttery, A. M. Garofalo, J. M. Hanson, R. J. La Haye, M. J. Lanctot, J.-K. Park, W. M. Solomon, and E. J. Strait, "The spectral basis of optimal error field correction on DIII-D," *Nucl. Fusion* (submitted).
- <sup>35</sup>J. E. Rice, I. Cziegler, P. H. Diamond, B. P. Duval, Y. Podpaly, M. Reinke, P. Ennever, M. Greenwald, J. W. Hughes, Y. Ma, E. Marmar, M. Porkolab, N. Tsujii, and S. M. Wolfe, *Phys. Rev. Lett.* **107**, 265001 (2011).
- <sup>36</sup>R. D. Gill, B. Alper, M. deBaar, T. C. Hender, M. F. Johnson, V. Riccardo, and Contributors to the EFDA-JET Workprogramme, *Nucl. Fusion* **42**, 1039 (2002).
- <sup>37</sup>J. H. Yu, E. M. Hollmann, N. Commaux, N. W. Eidiets, D. A. Humphreys, A. N. James, T. C. Jernigan, and R. A. Moyer, *Phys. Plasmas* **20**, 042113 (2013).
- <sup>38</sup>M. Bakhtiari, G. Kramer, M. Takechi, H. Tamai, Y. Miura, Y. Kusama, and Y. Kamada, *Phys. Rev. Lett.* **94**, 215003 (2005).
- <sup>39</sup>M. Landreman, A. Stahl, and T. Fulöp, *Comput. Phys. Commun.* **185**, 847 (2014).
- <sup>40</sup>A. Wingen, S. S. Abdullaev, K. H. Finken, M. Jakubowski, and K. H. Spatschek, *Nucl. Fusion* **46**, 941 (2006).
- <sup>41</sup>T. Kudyakov, S. S. Abdullaev, S. A. Bozhenkov, K. H. Finken, M. W. Jakubowski, M. Lehnen, G. Sewell, O. Willi, and Y. Xu, *Nucl. Fusion* **52**, 023025 (2012).
- <sup>42</sup>M. Forster, K. H. Finken, T. Kudyakov, M. Lehnen, O. Willi, Y. Xu, and L. Zeng, *Phys. Plasmas* **19**, 092513 (2012).
- <sup>43</sup>W. W. Heidbrink, *Rev. Sci. Instrum.* **57**, 1769 (1986).
- <sup>44</sup>A. N. James, E. M. Hollmann, and G. R. Tynan, *Rev. Sci. Instrum.* **81**, 10E306 (2010).
- <sup>45</sup>R. James, S. Janz, R. Ellis, D. Boyd, and J. Lohr, *Rev. Sci. Instrum.* **59**, 1611 (1988).
- <sup>46</sup>M. Brusati, D. V. Bartlett, and A. Ekedahl, *Nucl. Fusion* **34**, 23 (1994).
- <sup>47</sup>C. Fuchs and M. E. Austin, *Phys. Plasmas* **8**, 1594 (2001).
- <sup>48</sup>P. J. Catto, J. R. Myra, and A. J. Wootton, *Phys. Plasmas* **1**, 684 (1994).
- <sup>49</sup>P. Helander, L.-G. Eriksson, and F. Andersson, *Phys. Plasmas* **7**, 4106 (2000).
- <sup>50</sup>S. Abdullaev, K. H. Finken, T. Kudyakov, and M. Lehnen, *Contrib. Plasma Phys.* **50**, 929 (2010).
- <sup>51</sup>S. S. Abdullaev, K. H. Finken, and M. Forster, *Phys. Plasmas* **19**, 072502 (2012).
- <sup>52</sup>J. Zhang, W. A. Peebles, T. A. Carter, N. A. Crocker, E. J. Doyle, S. Kubota, X. Nguyen, T. L. Rhodes, C. Wannberg, and L. Zeng, *Rev. Sci. Instrum.* **83**, 10E321 (2012).
- <sup>53</sup>J. Zhang, N. A. Crocker, W. A. Peebles, T. A. Carter, and W. Guttenfelder, *Plasma Phys. Controlled Fusion* **55**, 045011 (2013).
- <sup>54</sup>A. B. Rechester and M. N. Rosenbluth, *Phys. Rev. Lett.* **40**, 38 (1978).
- <sup>55</sup>J. R. Myra, P. J. Catto, H. E. Mynick, and R. E. Duvall, *Phys. Fluids B: Plasma Phys.* **5**, 1160 (1993).
- <sup>56</sup>G. Papp, M. Drevlak, T. Fülöp, and P. Helander, *Nucl. Fusion* **51**, 43004 (2011).
- <sup>57</sup>V. A. Izzo, D. A. Humphreys, and M. Kornbluth, *Plasma Phys. Controlled Fusion* **54**, 095002 (2012).